



# Enhancing productivity and efficiency in conventional laser metal deposition process for Inconel 718 – Part II: advancing the process performance

Simone Maffia<sup>1</sup> · Federico Chiappini<sup>2</sup> · Gianluca Maggiani<sup>2</sup> · Valentina Furlan<sup>1</sup> · Massimo Guerrini<sup>2</sup> · Barbara Previtali<sup>1</sup>

Received: 13 June 2023 / Accepted: 19 August 2023

© The Author(s) 2023

## Abstract

This paper is the second part of a work focused on optimizing the performance of conventional Laser Metal Deposition (C-LMD) process for Inconel 718 (IN718). In Part I, through an extensive experimental campaign on single tracks, the interplay between process parameters and their impact on the deposition rate, powder catchment efficiency, and clad geometry is examined. The parameters investigated include laser power, scan speed, powder feed rate, and standoff distance. By systematically adjusting these parameters, the aim is to identify optimal conditions that maximize productivity while maintaining a favorable clad shape for multi-pass multi-layer depositions. Part II starts from the findings and results of Part I by continuing the optimization on thick wall structures. These are utilized to assess the effect of 3D geometrical process parameters, specifically hatch spacing and Z-step, on process performance and stability. Based on the findings, further optimization procedure is presented, pushing the boundaries of the C-LMD process for IN718. By fine-tuning the process parameters, the capability of the C-LMD process to deposit fully dense IN718 with a productivity of 1500 g/h and a powder catchment efficiency of 70% is demonstrated. These results highlight the potential of C-LMD as a viable manufacturing technique for efficiently fabricating large components. Overall, this study contributes to a deeper understanding of the relationship between process parameters and performance in C-LMD for IN718. The insights gained from this research can guide the development of efficient and cost-effective LMD strategies, facilitating the practical implementation of this process in various industries.

**Keywords** Laser metal deposition · Directed energy deposition · Productivity · Deposition rate · Efficiency · Optimization

## 1 Introduction

In the rapidly evolving field of additive manufacturing (AM), Laser Metal Deposition (LMD) has emerged as a versatile technique for fabricating complex geometries and repairing high-performance alloys [1]. Among these alloys, Inconel 718 (IN718), a nickel-based superalloy, has gained considerable attention due to its exceptional properties, including high strength at high temperatures, excellent corrosion resistance, and good thermal stability [2]. However,

even though the LMD process is often referred to as highly productive, the productivity of LMD for IN718 remains a critical factor that demands further investigation and optimization [3].

Productivity, which for LMD can be defined as the amount of material deposited per unit of time (i.e., the deposition rate), is a crucial metric in manufacturing processes. Achieving higher deposition rates means accelerating the fabrication process, making it economically viable for various industries as the lead time is reduced [4]. Indeed, due to the potentially high productivity the LMD process may reach, it is watched with interest by aerospace, oil and gas, and energy technology companies as a valid production technique for manufacturing large components with complex one-of-a-kind geometry [5]. The process is undoubtedly advantageous in these cases since no expensive molds are required and the stock material is limited, potentially leading

✉ Simone Maffia  
simone.maffia@polimi.it

<sup>1</sup> Department of Mechanical Engineering, Politecnico Di Milano, Via La Masa 1, 20156 Milan, Italy

<sup>2</sup> Nuovo Pignone Tecnologie S.R.L, Baker Hughes, Via Felice Matteucci 2, 50127 Florence, Italy

to material waste reduction in accordance to the modern sustainability standard requirements [6–8].

However, this is actually verified only if other factors are taken into account, such as the powder catchment efficiency (the ratio between the deposited material and the total amount of blown powder) and the absence of internal defects (like lack of fusion or unfavorable microstructure). Indeed, something that could happen while attempting to improve the productivity of the LMD process is that the powder catchment efficiency gets lower, as the provided energy is not enough to fully melt the delivered powder [9]. Furthermore, the required energy could be so high that it is not well dissipated by the component shape, damaging the microstructural quality of the material. In this last scenario, there may be a need to pause the deposition to allow the cooling of the part, which is detrimental to the overall productivity of the process [10].

In recent times, the theme of productivity of LMD was mainly addressed with the development of the high deposition rate LMD (HDR-LMD) process [11]. This approach includes the implementation of a special setup that allows for higher laser power (between 3000 and 7500 W), larger laser spots (diameter between 4 and 9 mm), and higher powder feed rates (between 3000 and 7000 g/h) than what is commonly used for the conventional LMD (C-LMD) process [9, 12–14]. These measures are indeed effective in improving productivity, but they come with some drawbacks, such as the need for special and expensive equipment, higher heat input to the component, and the need for new thermal models [15, 16]. On the other hand, the C-LMD process is arguably simpler to run as the necessary equipment is now standard, the heat input is typically low, and the heat treatments are extensively studied [2, 17, 18]. Still, the typical deposition rate of C-LMD (between 300 and 500 g/h for IN718) is often not enough to meet the manufacturing requirements for large components [19]. Another innovation in the field of high-productivity LMD technologies is the so-called Extreme High Speed Laser Application (EHLSA), a promising coating technology similar to C-LMD that promotes powder melting before reaching the substrate level. This process achieves very high scan speeds (between 10 and 100 m/min), which necessitates the use of specialized machine equipment. Although its use in laser cladding is now well established, with high deposition rates and powder catchment efficiency [20, 21], its use in 3D structures is still in its early stages. Indeed, as reported [22], the performance in realizing cuboids specimens is lower than with a C-LMD system due to the massive acceleration and deceleration required.

However, the productivity of C-LMD could still be enhanced from the current performance level with proper tuning of the process parameters aimed at optimization [23]. Optimizing the LMD process involves a multidimensional

exploration of parameters such as laser power, scanning speed, powder feed rate, standoff distance, laser spot diameter, hatch spacing, and the Z-step [24–28]. These parameters directly influence the microstructural characteristics of the material, its mechanical properties, and ultimately, the productivity and efficiency of the process [29–31]. Therefore, an in-depth understanding of the interplay between these variables and their impact on the deposition rate is essential for developing efficient and cost-effective LMD strategies for IN718.

Researchers usually address productivity and powder catchment efficiency separately [31–36], or together but with low deposition rates process conditions [37]. While certain attempts have been made to optimize the multi-objective C-LMD process [29], these efforts have not tackled the improvement of both productivity and powder catchment efficiency. Exploiting the particle bounce back effect on previously deposited clads, alternating the deposition of even and odd tracks is another interesting approach for increasing both productivity and powder catchment efficiency [38, 39]. This distinctive scanning strategy, however, may not always be feasible in practice. Finally, the evaluations and enhancements presented in the mentioned references primarily focus on the single track or single layer level (on a limited number of layers, i.e., laser cladding). To the best of the authors' knowledge, there are no published works that propose multi-objective performance optimization of the C-LMD process in terms of both productivity and powder catchment efficiency particularly in the context of thick-walled structures. This aspect, however, is critical in making the process attractive to an industrial audience [40, 41]. Productivity and powder catchment efficiency do not have the same relationship with the process input parameters, adding complexity to achieving simultaneous optimization.

The objective of this work is to investigate the factors influencing the productivity and the powder catchment efficiency of the C-LMD process for IN718 and propose optimization techniques to enhance these parameters. With a procedural series of experimental campaigns, the aim is to shed light on the underlying mechanisms that govern the deposition rate and the powder catchment and to identify key process parameters that significantly impact productivity. Alongside productivity, the proposed optimization procedure also considers the powder catchment efficiency and the internal quality of the deposited material, intended as the absence of lack of fusion porosity.

This work is divided into two parts. In Part I, an extensive investigation of the mechanisms linking the principal process parameters (laser power, scan speed, powder feed rate, and standoff distance) to the geometry of single tracks and process performance (i.e., productivity and efficiency) is proposed. By analyzing the data acquired with a 3D microscopy technique, an innovative approach for evaluating the

clad geometry and deposition performance was developed. By assessing the volume and geometry of the single tracks, a wealth of data was gathered to guide the optimization procedure. A multi-objective optimization method was applied to the data to find the best combinations of process parameters (among the tested ones) that maximize the C-LMD process performance by maintaining a favorable shape of the clad, in view of the multi-pass multi-layer depositions shown in Part II. The results of Part I showed that productivity between 700 and 800 g/h and efficiency of 75 to 90% are possible for the C-LMD process with IN718, while also maintaining the contact angle below 60°. However, the conclusions were that there is room for improvement, as the suggested process parameters were at the boundary of the tested experimental design.

The information and results gathered in Part I form the base for the further operations presented in Part II. The major hypothesis behind this work is that the optimization of the process performance can be performed on single tracks, as the principles regulating the productivity and efficiency on single clads will be the same for multi-pass multi-layer components, with only minor adjustments. In this Part II, thick wall specimens are realized to verify the effect of the 3D geometrical process parameters (i.e., hatch spacing and the Z-step) on the process performance. The optimization procedure is then finalized by extending the limits of process parameters tested in the previous steps, considering the gathered information. The final results show that C-LMD is capable of depositing fully dense IN718 with a productivity of 1500 g/h and a powder catchment efficiency of 70%, making the technology more appealing for the realization of large components.

## 2 Materials and methods

### 2.1 Powder and substrates

A plasma atomized Inconel 718 (IN718) alloy powder produced by AP&C—GE Additive (Saint Eustache, Canada) was used throughout this study. The nominal granulometry of this powder ranges between  $d_{10}=25$  and  $d_{90}=45$   $\mu\text{m}$ , and the alloy density is 8.17  $\text{g}/\text{cm}^3$  [42]. Refer to Part I of this work for more details about the powder.

The single-track depositions were performed on 10 mm thick AISI 304 substrates, while the thickness of the substrates used for thick wall depositions was 30 mm.

### 2.2 C-LMD system

The same C-LMD system described in Part I was used throughout this work. In brief, it is a CNC 5-axis LMD machine produced by SM Systems S.r.l. (Torre Canavese,

Italy), featuring an IPG Photonics YLS-4000 (Oxford, USA) active fiber laser source and a KUKA AG MWO-I-Powder (Augsburg, Germany) deposition head. A Sulzer Metco AG TWIN-10-C (Wohlen, Switzerland) is the employed powder feeder, and a Fraunhofer ILT COAX-40-F (Aachen, Germany) nozzle delivers the powder. Refer to Part I for the complete description and a picture of the system.

### 2.3 Single tracks characterization

The single-track specimens were acquired and analyzed with a newly developed methodology based on their acquisition with a 3D microscope and a semi-automatic processing algorithm to extract their width  $w$ , height  $h$ , contact angle  $\alpha$ , cross-section area  $A$ , and volume  $V_{st}$ . No cutting of the tracks is required with this method, and the intervention of the operator is minimal, allowing for a quick, robust and non-destructive comprehensive characterization of the deposition condition. Furthermore, the measures are conducted not only on a single cross-section of the track, like with the conventional method, but on a full portion of it, increasing the reliability of the measurement. The whole method is fully described in Part I of the work.

Generically speaking, starting from measuring the deposited volume, the productivity  $P$  (i.e., deposition rate) and the powder catchment efficiency  $E$  can be computed as in Eq. 1 and Eq. 2), respectively:

$$P = \frac{V * \rho * 60 * 60}{t * 1000}, \left[ \frac{\text{g}}{\text{h}} \right] \quad (1)$$

$$E = \frac{P}{pfr} * 100, [\%] \quad (2)$$

where  $\rho$  is the material density,  $V$  is the deposited volume,  $t$  is the deposition time and  $pfr$  is the powder feed rate. Equation 1 and Eq. 2) are the general definition of productivity and efficiency for the LMD process, regardless of sample type or deposition strategy [43–48]. Dealing with single tracks, the equation for the computation of  $P$  and  $E$  can be rewritten as in Eq. 3 and Eq. 4), respectively, and they are named  $P_{st}$  and  $E_{st}$ :

$$P = P_{st} = \frac{V_{st} * \rho * 60}{l/v * 1000}, \left[ \frac{\text{g}}{\text{h}} \right] \quad (3)$$

$$E = E_{st} = \frac{P_{st}}{pfr} * 100, [\%] \quad (4)$$

where  $l$  is the length of the acquired portion of the track, and  $v$  is the used scan speed. Further consideration about this computation is available in Part I.

### 2.4 Thick walls production and characterization

As part of the optimization procedure, thick multi-pass multi-layer straight walls were constructed. To emulate the realization of massive rotational components [49], a specific scanning strategy was created for the realization of the specimens. The approach is similar to the simpler zig scanning strategy, but includes oblique infill passes that alternate between odd and even layers. Each layer has one contour line on each side (for a total of two per layer), and the number of oblique infill lines is  $N_{il}$ . The walls are built vertically, with a fixed vertical distance between the levels known as Z-step  $Z_s$ . For all experimental phases, the length  $L$  of the walls is set at 180 mm. Figure 1 displays a visual representation of the scanning approach developed for each layer.

The thick walls are geometrically characterized by measuring their width  $W$  and height  $H$ . The width is averaged over three positions along the deposition direction. The height is measured twice (once per side to account for possible top surface inclinations) at each of the three positions along the deposition direction, where the width is also sampled, and then they are averaged. Figure 2 shows the thick wall measurement scheme.

These measures are helpful for quantifying deposition productivity and powder catchment efficiency. These are also defined by Eq. 1 and Eq. 2, as for the single tracks. The volume  $V$  and the deposition time  $t$  for thick walls, referred to as  $V_{tw}$  and  $t_{tw}$ , respectively, produced using the aforementioned scanning approach are computed as in Eq. 5 and 6. As a result, for thick walls, the productivity  $P$  takes the form of Eq. and is referred to as  $P_{tw}$ . Accordingly, the powder catchment efficiency  $E$  assumes the form of Eq. 8 and is referred to as  $E_{tw}$ .

$$V = V_{tw} = W * H * L, [mm^3] \tag{5}$$

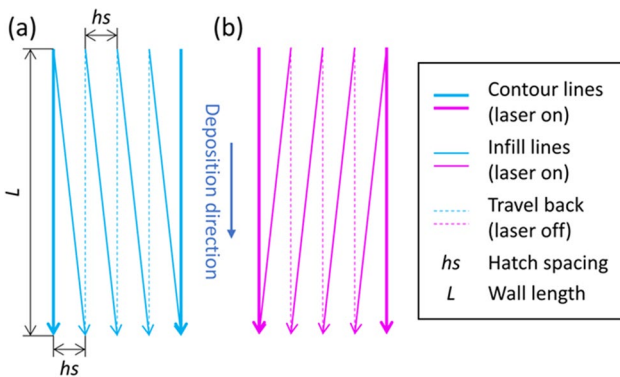


Fig. 1 Scanning strategy for thick multi-pass multi-layer straight walls: (a) odd layers; (b) even layers

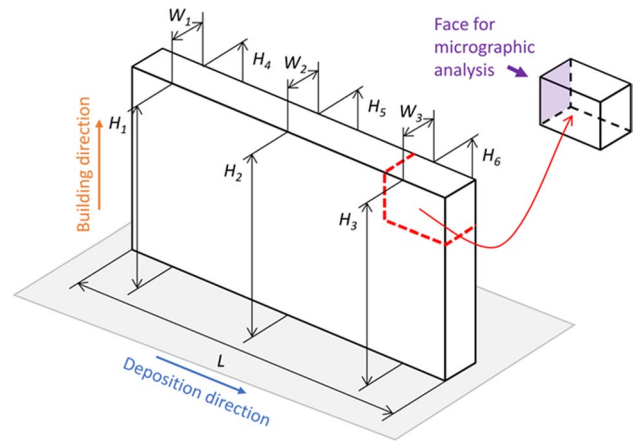


Fig. 2 Scheme of the geometrical measurements taken on the thick walls and representation of the cutting procedure (red dashed lines)

$$t = t_{tw} = \frac{L * (2 + N_{il}) * N_{la} * 60}{v}, [s] \tag{6}$$

$$P = P_{tw} = \frac{W * H * L * \rho}{\frac{L * (2 + N_{il}) * N_{la}}{v * 60} * 1000} = \frac{W * H * v * \rho * 60}{(2 + N_{il}) * N_{la} * 1000}, \left[ \frac{g}{h} \right] \tag{7}$$

$$E = E_{tw} = \frac{P_{tw}}{pfr} * 100, [%] \tag{8}$$

where  $N_{il}$  is the number of the oblique infill lines and  $N_{la}$  is the number of layers. Only the moments when the laser is active (i.e., when the deposition actually occurs) are included in the computation of the deposition time, and the oblique infill lines are considered parallel to the contour lines, ignoring transversal motion. In any case, given the relatively low ratio between hatch spacing  $hs$  and wall length  $L$ , the contribution of transversal motions to deposition time calculations is arguably negligible. The specimen length  $L$  does not show in the productivity computation for thick walls, since it is eliminated in the equation. Hence, the result can be readily expanded to longer specimens, or even more complicated components generated using the given scanning strategy. In any case, the reliance on  $N_{il}$  and  $N_{la}$  still remains. It should be noted, however, that  $W$  and  $H$  are both directly proportional to  $N_{il}$  and  $N_{la}$ . For this reason, as long as the specimen is high enough to activate the growing self-compensation effect [43], the result recorded at sample level can be extended to larger builds. One limitation of this approach is that the waviness of the sample is ignored. This could lead to an overestimation of the width, and thus of productivity and powder catchment efficiency. This effect, however, is mitigated by building a sufficiently large specimen.

The waviness is also limited due to the scanning approach used with contour lines at each layer.

Additionally, the thick walls are cut to reveal the transversal internal cross-section for micrographic inspection. The cut is made near the end of the deposition, getting only the last few layers, such that the process is already steady in both deposition and building directions. The cross-section is taken where there is the most overlap between the contours and adjacent infill lines. After the cutting step, the resulting specimen is hot mounted in resin, grinded and polished. Subsequently a cross-section image is captured to allow for the qualitative evaluation of porosity through optical inspection (i.e., assessing the presence and alignment of large pores, which are typical of inter-run lack of fusion defects). The analysis was also completed with a quantitative assessment of the apparent density. The cross-section images were imported into ImageJ [50] and a threshold was implemented to distinguish between pores and the denser material. The apparent density was computed as a percentage by dividing the area occupied by the dense material by the total evaluated cross-section area [51]. Additionally, the length of the major axis of the pores was evaluated when deemed necessary.

### 3 Process optimization procedure

The developed optimization procedure involves multiple sequential steps which can be divided into two main phases: the principal investigation and the further exploration. In the former phase, the links between the process parameters and the C-LMD process performance (i.e., productivity  $P$  and powder catchment efficiency  $E$ ) are established on single tracks (exploring the effects of the laser power  $p$ , the scan speed  $v$ , the powder feed rate  $pfr$  and the standoff distance  $sod$ ) and on thick walls (exploring the effect of the 3D process parameters, namely the hatch spacing  $hs$  and the Z-step  $Zs$ ). The findings of this first phase are then applied in the

further exploration of the C-LMD process performance, leading to the final optimization.

In Part I of this work, an extensive experimental campaign on single tracks (which is the initial investigation and optimization step, according to the scheme of Fig. 3) was carried out, and these will be discussed and applied in Part II.

#### 3.1 Refinement around best condition

While remaining at the single-track level, the solution (or solutions) derived from the previous response optimization procedure performed in Part I should be refined further by investigating the conditions surrounding it. Indeed, there is a significant difference between the levels of the factors investigated in the initial campaign, as the steps were 300 W for  $p$ , 180 mm/min for  $v$ , and 270 for  $pfr$ , and the experimented conditions were not replicated. For this reason, when the triplet  $(\hat{p}, \hat{v}, \hat{pfr})$  emerged as one of the best solutions from the initial investigation step, then the levels  $\hat{p} \pm 150$  W,  $\hat{v} \pm 90$  mm/min, and  $\hat{pfr} \pm 135$  g/h should be evaluated. A two-level three-factor full factorial experimental design with center point was used. Three replicates are realized for each corner condition, and six replicates are realized for the center point. The runs are randomized with the substrates acting as blocking factors. The  $sod$  was fixed to the highest of the two levels tested in the previous campaign, which is 9 mm. For each optimal solution to investigate, a total of 30 specimens are realized. The measured outputs from this campaign are the track width  $w$ , the track height  $h$ , the contact angle  $\alpha$ , the productivity  $P_{st}$ , and the powder efficiency  $E_{st}$ . For gathering these measurements, the developed method based on 3D microscopy was used. This is briefly described in Sect. 2.3. Refer to Part I for the in-depth description of the method.  $w$  and  $h$  are useful to tune the 3D geometrical process parameters (namely, the hatch spacing  $hs$  and the Z-step  $Zs$ ) necessary for the realization of the thick walls of the next step of the campaign.  $\alpha$ ,  $P_{st}$

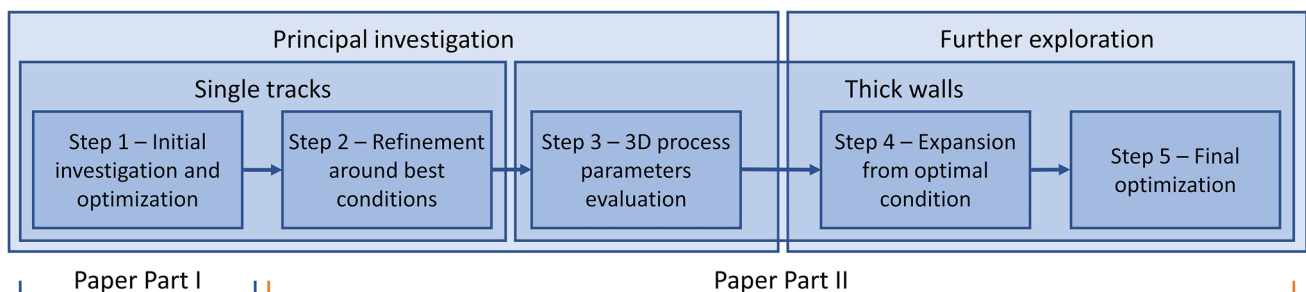


**Fig. 3** A scheme of the proposed process optimization procedure. The orange bracket identifies the steps covered in this Part II

and  $E_{st}$  are used to conduct further optimization using the approach discussed in Part I and based on composite desirability method. The arguments fed to the response optimizer were unchanged from the previous step:  $P_{st}$  and  $E_{st}$  must be maximized with the “weight” parameter set to 1 and the “importance” parameter set to 1.5 and 1, respectively. Furthermore, a constraint is set on the response  $\alpha$ , which must be  $< 60^\circ$ . In this step, only the linear terms were considered in the general linear model.

In the first step of the optimization procedure, reported in Part I, two sets of process parameters were identified as equally desirable: one with lower powder efficiency (around 78%) but higher productivity (around 818 g/h), and the other with higher powder efficiency (around 90%) but lower productivity (around 720 g/h). Both solutions were refined in this step, with two separate experimental campaigns conducted. As explained, the process parameters obtained as the best solutions from the initial investigation and optimization campaign presented in Part I are now used as the center points of the new two current campaigns. Table 1 and Table 2 list the process parameters for the two refinement experimental campaigns conducted in this step.

**Table 1** Process parameters of the refinement experimental campaign based on the optimization solution with lower efficiency and higher productivity

Fixed parameter	Level	
Laser spot diameter, [mm]	2.4	
Standoff distance, <i>sod</i> [mm]	9	
Varied parameters	Levels	Center point
Laser power, <i>p</i> [W]	1625; 1925	1775
Scan speed, <i>v</i> [mm/min]	1050; 1230	1140
Powder feed rate, <i>pfr</i> [g/h]	945; 1215	1080

**Table 2** Process parameters of the refinement experimental campaign based on the optimization solution with higher efficiency and lower productivity

Fixed parameter	Level	
Laser spot diameter, [mm]	2.4	
Standoff distance, <i>sod</i> [mm]	9	
Varied parameters	Levels	Center point
Laser power, <i>p</i> [W]	1625; 1925	1775
Scan speed, <i>v</i> [mm/min]	870; 1050	960
Powder feed rate, <i>pfr</i> [g/h]	675; 945	810

### 3.2 3D process parameter evaluation

Thick walls should be investigated for tuning the 3D geometrical process parameters: the hatch spacing *hs* and the Z-step *Zs*, starting with the refined results from the previous step on single tracks. To allow this passage, a fundamental assumption is made: a set of process parameters that realizes single tracks with high productivity will also realize thick walls with high productivity. As a result, the set of process parameters obtained through optimization on single tracks can be used directly for thick walls, provided a suitable combination of *hs* and *Zs* is chosen. The assessment of this hypothesis would be a significant benefit to the C-LMD process, as it would allow for the optimization of productivity at the single-track level (which is easier to handle and less expensive to make than thick walls), with time and economic benefits. As a result, a two-factor full factorial experimental campaign was chosen, with three levels for each factor. Hence, nine conditions are assessed.

Determining the appropriate 3D geometrical process parameters is fundamental to the success of LMD builds. Moving from a single layer deposition to a multi-pass deposition requires the careful determination of the degree of overlap between adjacent tracks to form the layer. Accordingly, the parameter *hs* is established. This parameter holds significant relevance within Laser Cladding (LC) applications, as it plays a direct role in shaping the undulations of the newly formed surface. Excessive *hs* leads to increase spacing between two adjacent tracks, resulting in diminished overlap and the emergence of pronounced valleys between them. Conversely, lower *hs* values yield thicker layers with reduced waviness [52]. Because productivity in LC is defined as the covered surface per unit time, the *hs* is critical in determining the balance between process performance and quality [41]. Shifting from single-layer multi-tracks LMD (i.e., LC) to multi-layer multi-tracks LMD, the *Zs* parameter should be determined. This parameter represents the increment of the distance between the initial substrate surface and the nozzle tip between the deposition of one layer and the subsequent one. An important consideration that should be made when dealing with the LMD process is that the *Zs* does not correspond to the layer thickness, unlikely with the Laser Powder Bed Fusion (LPBF) process. Ensuring a stable build necessitates aligning the *Zs* parameter as closely as possible with the average layer thickness. This average thickness results from a combination of factors: the dimensions (width, height, cross-section area) of the single clad, the chosen scanning strategy, and, ultimately, the *hs*, as previously discussed [53–55]. Consequently, these two 3D geometrical process parameters must be considered together when developing an LMD process, as their interplay holds primary significance. Failing to meet this requirement can

lead to the process deviating towards either undergrowth or overgrowth conditions.

Considering the used scanning strategy, the  $h_s$  is determined at around 50% of  $w$ . This value is a standard choice [29, 32, 37, 56, 57], due to its effective balance between the deposited layer thickness and the surface waviness [52]. Furthermore, by setting the  $h_s$  around 50% of  $w$ , the peak of the laser beam Gaussian power distribution is aligned on the boundary of the previously deposited track, thus minimizing the risk of inter-run porosity [24]. With  $h_s$  established, the  $Z_s$  is subsequently configured to center the full factorial experimental plane around stable process conditions. The suitable range of  $Z_s$  was explored through preliminary experimentation to determine the feasibility window. It is also noteworthy that the layer thickness changes during deposition due to the self-regulation effect inherent in the LMD process [43]. Consequently, preliminary experimentations to find the suitable levels of  $Z_s$  are usually required. For  $h_s$  fixed at 50% of  $w$ , the applicable  $Z_s$  range was identified to be between 130 and 160% of  $h$  for the used scanning strategy. In this step, to evaluate the process growth stability, the target number of layers  $N_{la}$  was set to 25, and the number of oblique infill lines  $N_{il}$  was set to 3.

The specimens were first evaluated based on their growth, which was classified as undergrowth if it were lower than expected, overgrowth if it was higher than expected, and good growth if it was close to the expected height. By multiplying  $Z_s$  by  $N_{la}$ , the expected height is calculated. Both undergrowth and overgrowth are undesirable conditions. When undergrowing occurs, it means that the layer height is lower than the imposed  $Z_s$ , and the build is lost after a few layers. When overgrowth occurs, on the other hand, the layer height is greater than  $Z_s$ . In this case, after a few layers, the powder catchment efficiency decreases because the laser beam no longer intercepts the powder stream well [53], and the self-regulating phenomenon of the C-LMD process is enabled, stabilizing the growth [43, 58]. However, if the

overgrowth is too high, the molten pool gets too close to the nozzle tip, which can damage the nozzle and cause powder clogging in the nozzle meatus, requiring the deposition to be stopped [24]. The successful builds (those that reached the target number of layers) were characterized using the method described in Sect. 2.4, by estimating productivity and powder catchment efficiency based on width and height measurements. As explained, the internal porosity was also evaluated to assure the internal quality.

Three process conditions were identified as optimal from the previous step, and a separate experimental campaign was designed for each of them. The process parameters of these are reported in Table 3.

This step completes the principal investigation phase of the proposed work, in which single track experiments were used to determine the receipt for obtaining high productive process conditions, and thick walls were used to tune the 3D geometrical parameters for ensuring stable and porosity-free builds. This optimization procedure, however, is limited to the tested range of process parameters, and two of the investigated process parameters reached the maximum value. This suggests that if there is a possibility of increasing these, it may be beneficial. As a result, the information gathered in this phase can be verified beyond the range to further improve process performance.

### 3.3 Expansion from optimal condition

As with the previous dissertation, moving the process parameters beyond the investigated ranges should improve process performance even further. However, the tested  $p$  was already close to the maximum level allowed by the used setup to run smoothly, despite experimental evidence suggesting that increasing  $p$  would be a benefit for both  $P$  and  $E$ . As a result, beginning with the best condition discovered during the primary experimental campaign,  $v$  and  $pfr$  were independently increased without changing the other process parameters, and  $p$  was set to 2000 W. A factorial experimental campaign

**Table 3** Process parameters of the three designed experimental campaign for the investigation of the 3D geometrical parameters

	Condition 1.1	Condition 1.2	Condition 2.1
Fixed parameter	Level	Level	Level
Laser spot diameter, [mm]	2.4	2.4	2.4
Standoff distance, $sod$ [mm]	9	9	9
Laser power, $p$ [W]	1925	1925	1925
Scan speed, $v$ [mm/min]	1050	1230	870
Powder feed rate, $pfr$ [g/h]	1215	1215	945
Varied parameters	Levels	Levels	Levels
Hatch spacing, $h_s$ [mm]	1.30; 1.50; 1.70	1.10; 1.30; 1.50	1.30; 1.50; 1.70
Z-step, $Z_s$ [mm]	1.15; 1.25; 1.35	1.15; 1.25; 1.35	1.15; 1.25; 1.35

was not designed in this case because it was expected that the behavior of the process parameters would not deviate significantly from what was observed in the primary campaign, thereby reducing the number of samples required. During this phase, both single tracks and thick walls were realized and characterized using the previously discussed methods. Taking into account the findings of the initial investigation and optimization campaign reported in Part I of this work, the increase in  $v$  appears to be beneficial to the shape of the track (i.e., the contact angle  $\alpha$ ) but not to  $P_{st}$ . This should be checked during this step. An important aspect that is faced in this phase is the evaluation of the internal quality of the specimens in terms of inter-run lack of fusion porosity. As the constraint on the maximum  $\alpha$  was suspended to assess higher levels of  $pfr$ , the risk of the onset of this defect could increase. Both quantitative and qualitative evaluations of the porosity were conducted.

The geometrical characterization of single tracks is used not only to validate the results obtained in the primary experimental campaign beyond the previously tested boundaries, but also to fine-tune  $hs$  and  $Zs$  of thick walls produced using the same process parameters. Because of the observations made in the previous step,  $hs$  was set to 60% of  $w$  and  $Zs$  to 110% of  $h$  in the 3D geometrical parameters. Table 4 summarizes the process parameters of these  $v$  and  $pfr$  experiments. The number of oblique infill lines  $N_{il}$  was set to 3, unchanged from the previous step, while the number of layers  $N_{la}$  was reduced to 15, since it was observed that this value is enough to allow them to reach the steady state of the build.

### 3.4 Final optimization

The knowledge gained about the effect of process parameters on the measured outputs and their interaction is put into practice in this final step. A final experimental campaign was

designed to investigate the onset of pores in the samples with increased  $pfr$ . Indeed, by varying  $pfr$  on its own in the previous step,  $P_{tw}$  increased, but so did  $\alpha$ , which moved well above the empirical limit established for the initial investigation and optimization step. This is the cause of the formation of lack of fusion pores, as discussed in the following sections and considering the results and their discussion. Another hypothesis that needs to be confirmed is the role of  $v$ . Indeed, the previous steps demonstrated that  $v$  has a significant effect on  $h$  and on  $\alpha$  of the deposited track, but it has little effect on  $P_{st}$  and on  $E_{st}$ .

For ultimately proving these two hypotheses and to finalize the optimization procedure, a final experiment was designed again by varying  $v$  and  $pfr$  in a simple factorial campaign with two levels. The number of oblique infill lines  $N_{il}$  and the number of layers  $N_{la}$  remained unchanged from the previous experimental campaign, and were fixed to 3 and 15, respectively. The porosity was evaluated both qualitative and quantitative. Table 5 collects the process parameters of this final campaign.

**Table 5** Process parameters for the finalization of the optimization procedure

Fixed parameter	Level
Laser spot diameter, [mm]	2.4
Standoff distance, $sod$ [mm]	9
Laser power, $p$ [W]	1925
Hatch spacing, $hs$ [mm] (only thick walls)	60% of $w$
Z-step, $Zs$ [mm] (only thick walls)	110% of $h$
Varied parameters	Levels
Scan speed, $v$ [mm/min]	1230; 1980
Powder feed rate, $pfr$ [g/h]	1965; 2115

**Table 4** Process parameters for the further investigation of  $v$  and of  $pfr$

	Investigation of $v$	Investigation of $pfr$
Fixed parameter	Level	Level
Laser spot diameter, [mm]	2.4	2.4
Standoff distance, $sod$ [mm]	9	9
Laser power, $p$ [W]	2000	2000
Scan speed, $v$ [mm/min]	-	1230
Powder feed rate, $pfr$ [g/h]	1215	-
Hatch spacing, $hs$ [mm] (only thick walls)	60% of $w$	60% of $w$
Z-step, $Zs$ [mm] (only thick walls)	110% of $h$	110% of $h$
Varied parameters	Levels	Levels
Scan speed, $v$ [mm/min]	1230; 1380; 1530; 1680; 1830	-
Powder feed rate, $pfr$ [g/h]	-	1215; 1365; 1515; 1665; 1815



## 4 Results

### 4.1 Refinement around best condition

Because two optimal solutions were chosen in the initial investigation and optimization step, shown in Part I, two separate experimental campaigns were required for result refinement, and the process parameters are listed in Table 1 and Table 2. Each experimental campaign required the deposition of 30 single tracks, needing two substrates. Figure 4 shows the pictures of the produced samples.

The ANOVA tables of  $w$ ,  $h$ ,  $\alpha$  and  $A$  are collected in the supplementary information. Table 6 and Table 7 report the results of the analyses of  $P_{st}$  and  $E_{st}$  of the experiments around solution 1, respectively, while Table 8 and Table 9 show the ones of the experiments around solution 2. In all the cases, the standardized residuals were normally distributed, and the tests for equal variances were verified. The blocking factors turned out to be significative in the

analyses. Thus, they were considered in the general model for the optimization.

Figure 5 shows the cube plots of the fitted and averaged responses. The effects of the process parameters are no longer as noticeable in the tested ranges as they were in the previous larger campaign, especially when  $E_{st}$  is considered. Indeed, the model summaries of the analyses of  $E_{st}$  show lower coefficients of determination. This could be because the variability of  $E_{st}$  in these experiments is low. Nonetheless, the analysis is valid and can be applied to the optimization strategy. An intriguing fact is that  $p$ , which was significant for both  $P_{st}$  and  $E_{st}$  in the initial experimental campaign, has no effect on these responses in this narrow range of process parameters. Furthermore,  $v$  is important in determining  $E_{st}$  around solution 2.

For the two refinement experimental campaigns, the three best solutions provided by the composite desirability method using the input parameters in Sect. 3.1 are listed in Table 10 and .

**Fig. 4** The single tracks of the refinement experimental campaign

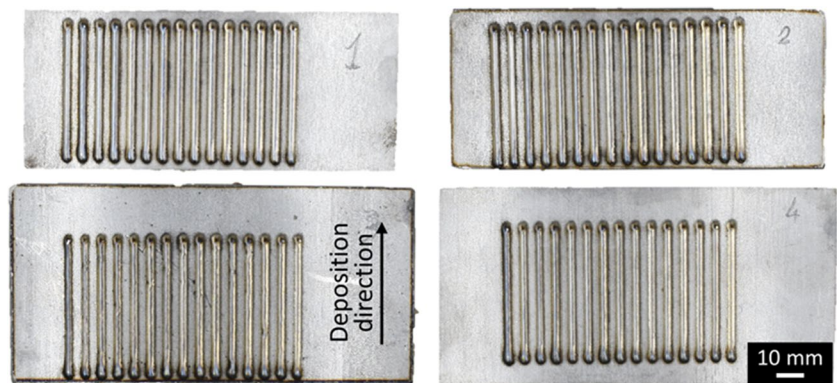


**Table 6** ANOVA table for the productivity of single tracks of the refinement campaign around solution 1

Source	DF	Adj SS	Adj MS	F-value	P-value	Significant
Model	5	248179	49636	25.36	0.000	x
Blocks	1	86657	86657	44.27	0.000	x
Linear	3	161518	53839	27.5	0.000	x
$p$	1	3077	3077	1.57	0.222	
$v$	1	383	383	0.20	0.662	
$pfr$	1	158058	158058	80.75	0.000	x
Curvature	1	4	4	0.00	0.966	
Error	24	46979	1957			
Lack-of-Fit	4	1415	354	0.16	0.958	
Pure Error	20	45563	2278			
Total	29	295158				

Model summary			
S	R-sq [%]	R-sq(adj) [%]	R-sq(pred) [%]
44.2431	84.08	80.77	75.13

**Table 7** ANOVA table for the powder catchment efficiency of single tracks of the refinement campaign around solution 1

Source	DF	Adj SS	Adj MS	F-value	P-value	Significant
Model	5	933.26	186.652	10.81	0.000	x
Blocks	1	769.57	769.573	44.58	0.000	x
Linear	3	163	54.335	3.15	0.044	x
$p$	1	23.75	23.751	1.38	0.252	
$v$	1	2.64	2.636	0.15	0.699	
$pfr$	1	136.62	136.617	7.91	0.010	x
Curvature	1	0.68	0.685	0.04	0.844	
Error	24	414.33	17.264			
Lack-of-Fit	4	25.54	6.385	0.33	0.856	
Pure Error	20	388.78	19.439			
Total	29	1347.59				

Model summary			
S	R-sq [%]	R-sq(adj) [%]	R-sq(pred) [%]
4.15494	69.25	62.85	51.96

Table 11. In both cases, the highest level of  $p$  and  $pfr$  is recommended to achieve the best results. The results of this refinement step in terms of  $P_{st}$  and  $E_{st}$  were only slightly improved over the initial optimization campaign, but they are still arguably promising.

These results are still at the single-track level, and they should be tested in the realization of multi-track multi-layer thick wall samples to assess the validity of the initial hypothesis behind this optimization procedure (i.e., deposition conditions that are highly productive and efficient for producing single tracks are highly productive and efficient in depositing multi-track multi-level components). As a result, two solutions from Table 10 (solution 1.1 and 1.2) and one from .

Table 11 (solution 2.1) were considered. The first two conditions should have a deposition rate of around 900 g/h and a powder catchment efficiency of 75%. Based on the findings, it was decided to investigate both solutions in order to assess the effect of  $v$  in the deposition of thick walls. Indeed, while  $v$  has little to no impact on  $P_{st}$  and  $E_{st}$ , it has a strong influence on the geometry and cross section area of the clad, which can be useful in some situations. Solution 2.1 stands out in terms of powder catchment efficiency, with values exceeding 90%, paired with high productivity. As a result, it was chosen to be tested on thick walls. Table 12 shows the predicted responses and 95% confidence intervals for the three selected solutions.

**Table 8** ANOVA table for the productivity of single tracks of the refinement campaign around solution 2

Source	DF	Adj SS	Adj MS	F-value	P-value	Significant
Model	5	327,081	65,416	91.73	0.000	x
Blocks	1	14,706	14,706	20.62	0.000	x
Linear	3	315,738	105,246	147.57	0.000	x
$p$	1	314	314	0.44	0.513	
$v$	1	13,443	13,443	18.85	0.000	x
$pfr$	1	307,695	307,695	431.44	0.000	x
Curvature	1	4420	4420	6.20	0.020	x
Error	23	16,403	713			
Lack-of-Fit	4	1442	361	0.46	0.766	
Pure Error	19	14,961	787			
Total	28	343,484				

Model summary			
S	R-sq [%]	R-sq(adj) [%]	R-sq(pred) [%]
26.7053	95.22	94.19	92.43

**Table 9** ANOVA table for the powder catchment efficiency of single tracks of the refinement campaign around solution 2

Source	DF	Adj SS	Adj MS	F-value	P-value	Significant
Model	5	469.96	93.992	8.32	0.000	x
Blocks	1	216.456	216.456	19.17	0.000	x
Linear	3	215.449	71.816	6.36	0.003	x
<i>p</i>	1	4.077	4.077	0.36	0.554	
<i>v</i>	1	213.741	213.741	18.93	0.000	x
<i>pfr</i>	1	0.39	0.39	0.03	0.854	
Curvature	1	66.424	66.424	5.88	0.024	x
Error	23	259.742	11.293			
Lack-of-Fit	4	28.547	7.137	0.59	0.676	
Pure Error	19	231.195	12.168			
Total	28	729.702				

Model summary

S	R-sq [%]	R-sq(adj) [%]	R-sq(pred) [%]
3.36053	64.40	56.67	43.60

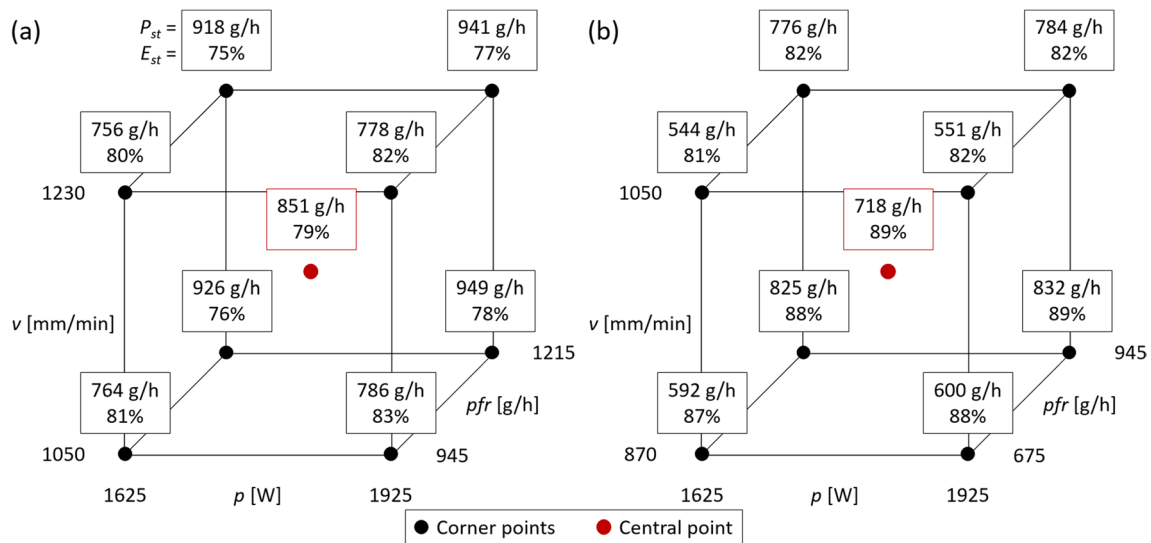


**Fig. 5** Cube plots of productivity and powder catchment efficiency fitted and mediated on the blocks: (a) solution 1; (b) solution 2

**Table 10** The three best solutions of the optimization method for the refinement campaign around solution 1

Solution	<i>p</i> [W]	<i>v</i> [mm/min]	<i>pfr</i> [g/h]	$\alpha$ [deg]	$P_{st}$ [g/h]	$E_{st}$ [%]	Composite desirability
1.1	1925	1050	1215	56.5	949	78	0.59
1.2	1925	1230	1215	52.7	941	77	0.58
1.3	1775	1140	1080	53.9	851	79	0.48

**Table 11** The three best solutions of the optimization method for the refinement campaign around solution 2

Solution	$p$ [W]	$v$ [mm/min]	$pfr$ [g/h]	$\alpha$ [deg]	$P_{st}$ [g/h]	$E_{st}$ [%]	Composite desirability
2.1	1925	870	945	56.7	832	89	0.78
2.2	1775	960	810	52.3	718	89	0.61
2.3	1925	1050	945	51.5	783	82	0.55

**Table 12** Selected solutions of the refinement step with the predicted responses

	Solution 1.1		Solution 1.2		Solution 2.1	
$p$ [W]	1925		1925		1925	
$v$ [mm/min]	1050		1230		870	
$pfr$ [g/h]	1215		1215		945	
	Prediction	95% CI	Prediction	95% CI	Prediction	95% CI
$w$ [mm]	2.82	2.79–2.85	2.72	2.68–2.75	3.01	2.97–3.04
$h$ [mm]	0.92	0.89–0.96	0.82	0.79–0.86	0.96	0.93–0.99
$\alpha$ [deg]	56.5	54.2–58.8	52.7	50.4–55.0	56.7	55.0–58.4
$A$ [mm <sup>2</sup> ]	1.83	1.76–1.90	1.57	1.50–1.64	1.93	1.88–1.98
$P_{st}$ [g/h]	949	911–986	940	903–978	856	809–855
$E_{st}$ [%]	78	75–82	77	74–81	91	86–91

### 4.2 3D process parameters evaluation

The three experimental campaigns of this step produced 9 thick wall specimens each, for a total of 27 specimens. Figure 6 show pictures of the deposited samples. Figure 7 collects the images of the cross-sections of the thick walls, with the indication of the build outcome (correct growth, undergrowth and overgrowth),  $P_{tw}$  and  $E_{tw}$ . Missing pictures means that the build failed with that combination of  $hs$  and  $Zs$ .

The first thing to notice is that the process window of the 3D geometrical parameters appears to be narrow, with only a few possible combinations. Furthermore,  $hs$  and  $Zs$  should be adjusted in tandem to avoid problems with sample growth. When these two are well tuned to achieve proper growth,  $P_{tw}$  and  $E_{tw}$  do not change significantly.

Furthermore, the obtained levels of  $P_{tw}$  and  $E_{tw}$  are interestingly higher than what was obtained with the single tracks realized with the same process parameters. Increased process performance in depositing thick walls could be due to a variety of factors, including overall heat accumulation in the working area, whereas the substrate was always cool during single track realization. Moreover, it should be noted that the developed method for measuring  $P_{tw}$  and  $E_{tw}$  of thick wall samples slightly overestimates the results because it is based on the deposited wall being approximated as a perfect rectangular prism. Nonetheless, the error is small due to the sample dimensions, and is negligible. Finally, almost no porosity was observed in the cross-sections, except for a few sporadic cases. The well-grown samples are fully dense, (with a measured apparent density consistently above



**Fig. 6** The thick wall samples realized for the 3D process parameters evaluation step

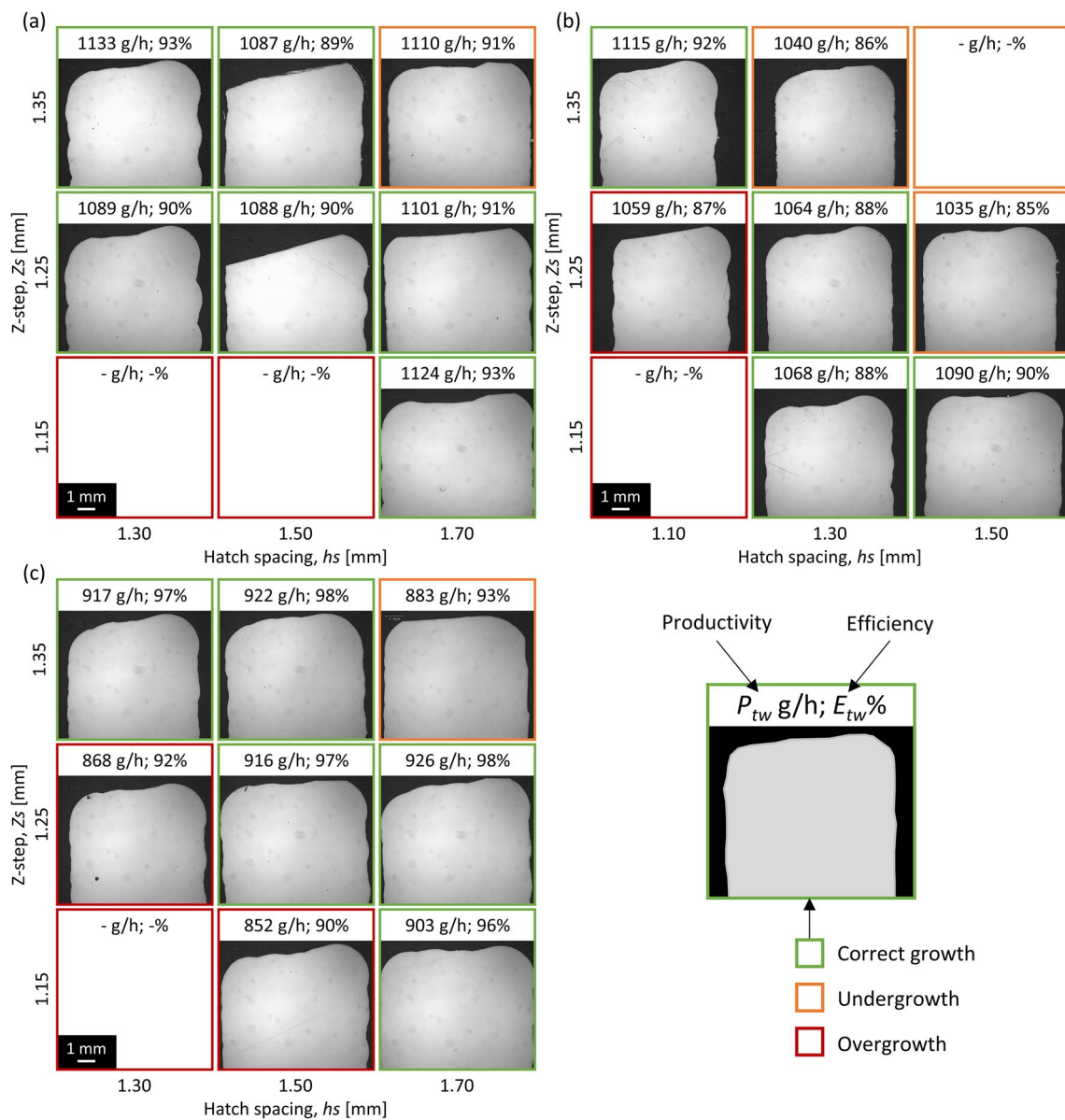


**Fig. 7** Cross-section of the thick wall samples of the three experimental conditions for the 3D process parameters evaluation: (a) condition 1.1; (b) condition 1.2; (c) condition 2.1

99.98%), indicating that the constraint on  $\alpha$  of the single tracks was correctly set.

The average values of  $P_{tw}$  and  $E_{tw}$  obtained for the three tested conditions are collected in Table 13 (only the correctly grown specimens were considered, as the overgrown and undergrown conditions should be discarded). Reflecting the results obtained on single tracks, the deposition rate was higher in conditions 1.1 and 1.2, but the powder catchment efficiency was higher in condition 2.1, nearly melting all the delivered powder. The reason for evaluating both conditions 1.1 and 1.2 was to investigate the effect of  $v$  on process performance. The Mann–Whitney  $U$  test was used to determine whether the average  $P_{tw}$  obtained in

the first two conditions was the same or not. The obtained  $p$ -value is 0.352, confirming that  $v$  has no effect on the deposition rate, at least not in the tested range (1050 mm/min; 1230 mm/min).

**Table 13** Average ( $\pm$ standard error of the mean) productivity and efficiency obtained with the three tested deposition conditions

Condition	$P$ [g/h]	$E$ [%]
1.1	1104 $\pm$ 8	90.8 $\pm$ 0.7
1.2	1084 $\pm$ 12	89.2 $\pm$ 1.0
2.1	917 $\pm$ 4	97.0 $\pm$ 0.4

The principal investigation phase of the optimization procedure is completed with these results. The proposed method was shown to be effective in generating sets of process parameters that determine high deposition rates, high powder catchment efficiency, and full dense deposited material. The actual optimization was conducted primarily on single tracks, and the results were applied to thick wall samples, where only the 3D geometrical process parameters were tuned to ensure a build without process drift or failure. Although the results are promising, they are limited to the tested ranges of process parameters investigated on the single tracks, as extrapolation of results is not recommended. Nonetheless, the solutions of the optimization method indicate that there is still room for improvement, and this is assessed with the following steps belonging to the further exploration phase of the procedure.

### 4.3 Expansion from optimal condition

This step examined the influence of  $v$  and  $pfr$ . Even though the experimental evidence suggested that it would be beneficial for the enhancement of  $P$  and  $E$ ,  $p$  was not further investigated because the maximum level required to run the process smoothly was reached. The same process parameters were used to deposit both single tracks and thick walls, and specimen images are included in Fig. 8.

The single tracks were acquired and characterized in the same manner as in the previous steps: Fig. 9 depicts the

reconstructed cross-sections of the single tracks deposited by varying  $v$  and  $pfr$ , while Fig. 10 collects the measured quantities, summarizes the measured quantities. The results exhibit the same patterns as those seen in previous experiments with lower levels of  $v$  and  $pfr$ :

- Increasing  $v$  reduces both  $w$  and  $h$ , particularly the latter. This reduces  $A$  as well as  $\alpha$ . Because the decrease in  $A$  is offset by the increase in  $v$ , the amount of material deposited per unit of time (i.e.,  $P_{st}$ ) is unaffected and oscillates between 900 and 1000 g/h. Because the  $pfr$  remains constant between runs,  $E_{st}$  is also unaffected, oscillating between 70 and 80%.
- Increasing  $pfr$  affects only  $h$  and has no effect on  $w$ . As a result, as  $pfr$  increases, so does  $\alpha$  and  $A$ . The increase in  $A$  without changing  $v$  results in an increase in  $P_{st}$ , which ultimately reached 1200 g/h. However, the powder catchment efficiency  $E_{st}$  has deteriorated and has fallen below 70%.

With this experiment on single tracks, remarkably high values of  $P_{st}$  were obtained by increasing the  $pfr$ . However,  $\alpha$  becomes too steep. When depositing multi-pass multi-layer components, the overlap of clads with such profiles may prevent proper melting of the material, resulting in the formation of lack of fusion porosity between adjacent tracks. Regardless, thick walls were deposited using these process parameters to validate the assumption.

**Fig. 8** The samples realized for the exploration of process parameters beyond the ranges assessed in the primary campaign: (a) single tracks and (b) thick walls

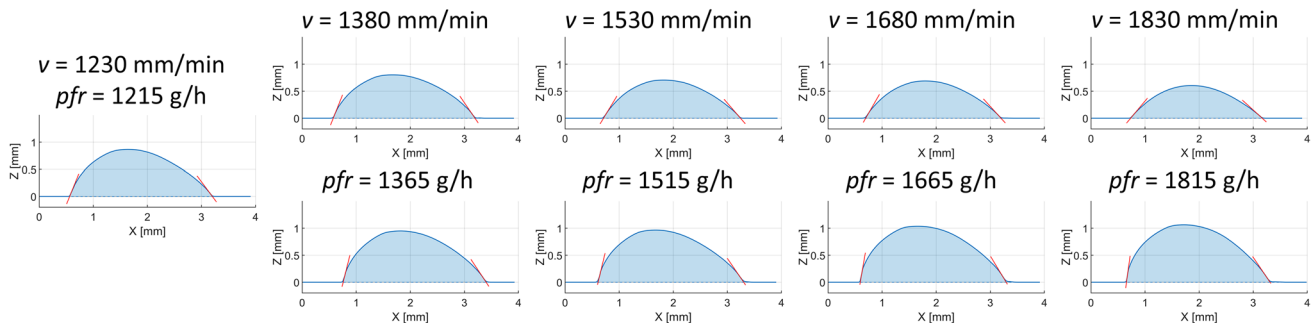
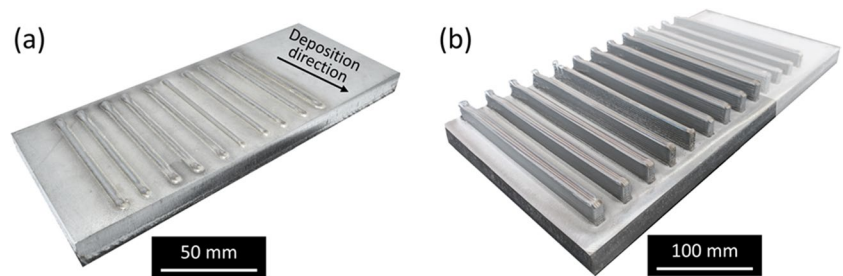


**Fig. 9** Reconstructed cross-sections of the single tracks deposited by varying the scan speed and the powder feed rate

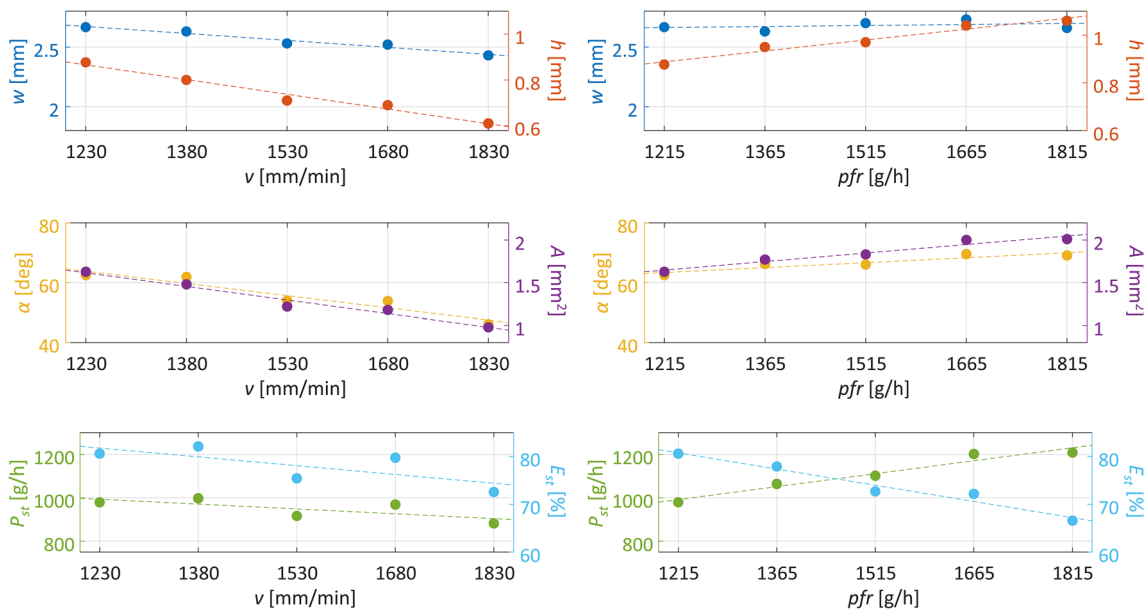


Fig. 10 Graphs of the responses measured on the single tracks deposited by varying the scan speed and the powder feed rate (lines of best fit plotted on top of the data)

Figure 11 shows the cross-sections of the thick-walled samples, and Fig. 12 shows the measured  $P_{tw}$  and the  $E_{tw}$  in the tested conditions. The behavior of thick walls closely resembles that of single tracks: variations in  $v$  exhibit minimal influence on the outcomes, whereas increases in  $pfr$  lead to a noteworthy

rise in  $P_{tw}$  alongside a minor reduction in  $E_{tw}$ . Consequently, the observed trends are consistent. As already observed in the previous experimental step, the process performance is slightly yet significantly higher than with the corresponding single track, particularly under conditions with high  $v$  or high  $pfr$ .

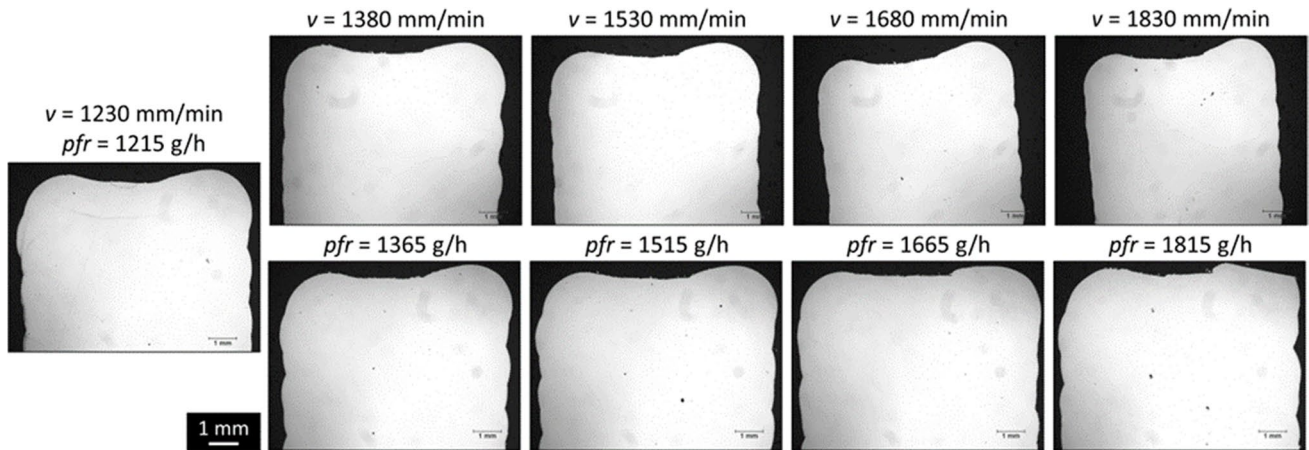


Fig. 11 Cross-sections of the thick walls deposited by varying the scan speed and the powder feed rate

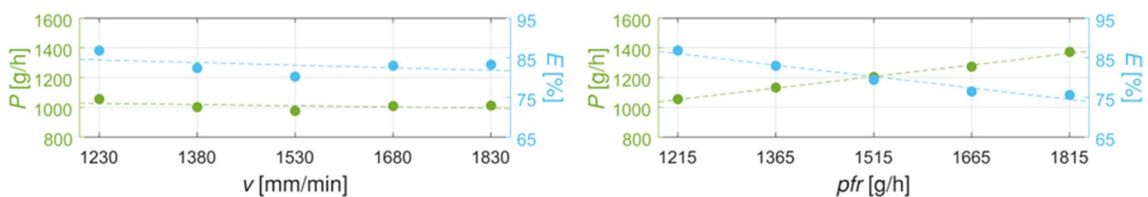


Fig. 12 Graphs of the productivity and efficiency measured on the thick walls deposited by varying the scan speed and the powder feed rate (lines of best fit plotted on top of the data)

However, as anticipated, the steeper  $\alpha$  achieved in single tracks at elevated levels of  $pfr$  resulted in the occurrence of inter-run lack of fusion porosity. Given that the pores are well aligned, and their position coincides with the overlap of adjacent clads, this assertion can be made. Despite this occurrence, the apparent density of all samples surpasses 99.95%, and the largest pore measures merely 0.14 mm in length. Consequently, although process performance exhibits enhancement, there is a minor degradation in the internal quality of the deposition.

To complete the study, the increments of  $v$  and  $pfr$  should be combined. The latter would improve process performance in terms of  $P_{tw}$  while decreasing the internal quality of the deposited material. The former would resolve the internal porosity issue while maintaining process performance.

#### 4.4 Final optimization

A two-factor, two-level experimental campaign was conducted to investigate the combined roles of  $v$  and  $pfr$  in determining process performance ( $P_{tw}$  and  $E_{tw}$ ) and the density of the deposited multi-pass multi-layer components. Figure 13 depicts the four thick walls of this experiment, while Fig. 14 depicts the cross-sections as well as  $P_{tw}$  and  $E_{tw}$ .

The inter-run lack of fusion voids is clearly present in the cross-sections when the lowest level of  $v$  is used, whereas when the higher level of  $v$  is used, the deposited material is completely dense, with no presence of pores. The apparent density of both samples dropped to 99.87%, with the largest pores measuring 0.35 mm in length. Indeed, with such high levels of  $pfr$ , the shape of the single clad would be too steep unless offset by a sufficiently high level of  $v$ . Furthermore, while the increase in  $v$  is significant in this experimental plan, its effect on the  $P_{tw}$  and  $E_{tw}$  is marginal. As a result, the evidence supports all of the hypotheses.

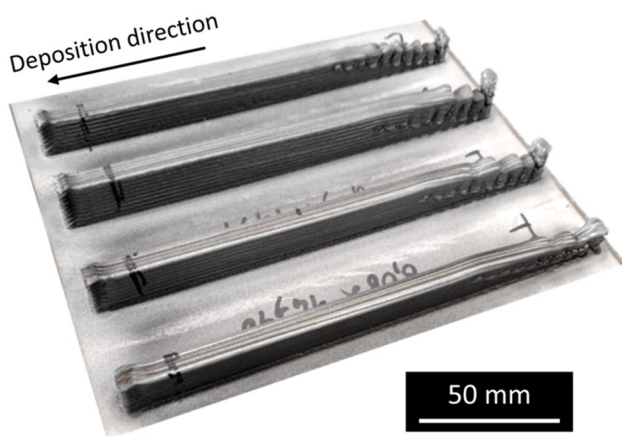


**Fig. 13** The four specimens deposited with both high levels of scan speed and powder feed rate

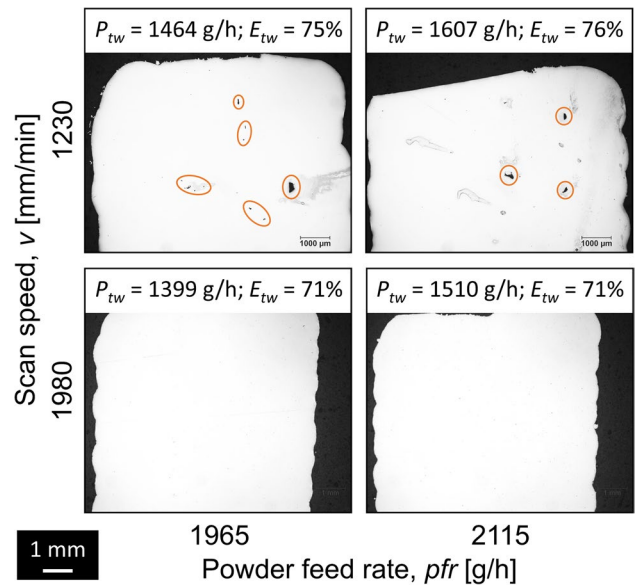


**Fig. 14** Cross-sections of the thick walls deposited with both high levels of scan speed and powder feed rate with productivity and efficiency values for each condition. The orange ovals identify the inter-run lack of fusion pores

## 5 Discussion

To address the theme of the performance of the C-LMD process, a step-by-step experimental procedure was devised involving the deposition and analysis of single tracks and of multi-pass multi-layer thick walls. The work was divided into two parts. In Part I, the initial investigation and optimization experimental campaign on single tracks was reported. It assessed the primary effects of the process parameters on the track geometry, on the productivity  $P_{st}$ , and on the efficiency  $E_{st}$ . The laser power  $p$  was found to strongly influence both  $P_{st}$  and  $E_{st}$ , and the  $pfr$  was the most significant parameter on  $P_{st}$ . However, if the  $pfr$  is too much increased,  $E_{st}$  can be badly affected by it, and most importantly the contact angle  $\alpha$  becomes too steep (which is a potential source of lack of fusion in thick wall depositions). The scan speed  $v$  has a remarkable impact on the track geometry, especially by reducing  $\alpha$  when increased, but it seems to have no effect on both  $P_{st}$  and  $E_{st}$ . This is because the cross-section area  $A$  gets smaller by raising  $v$ . Hence, the two effects of traveling faster and reducing  $A$  counteract with each other, resulting in an unchanged deposition rate. As a conclusion of Part I, a multi-objective optimization procedure was conducted seeking the combinations of process parameters which provide the best combinations of high  $P_{st}$  and  $E_{st}$ , by maintaining a reasonably low level of  $\alpha$ . Two groups of solutions resulted as equally valid for the set criteria: one having the highest levels of  $P_{st}$  by slightly sacrificing  $E_{st}$ , and the second one promoting the highest levels of  $E_{st}$ , but with a slightly lower  $P_{st}$ .



In Part II of the work, it was decided to investigate both proposed groups of solutions further, bringing the two best results from Part I to the following steps. The results of the two refinement campaigns revealed slightly different relationships between the tested process parameters and the responses, with respect to what was observed in Part I. Indeed,  $p$  was no longer having a significant impact on both  $P_{st}$  and  $E_{st}$ , and  $v$  played a role in the resulting  $E_{st}$  in the campaign centered on solution 2, which achieved higher levels of  $E_{st}$ . It should be noted that the  $E_{st}$  has an upper limit of 100%, which means that the laser melts all the delivered powder and there is no waste. The obtained deposition conditions are surprisingly close to this limit, and the behavior is no longer as simple as it was for lower levels of  $E_{st}$ . More research should be done to determine the deposition conditions that determine the complete catchment of sprayed powder. Nonetheless, this refinement passage slightly improved process performance, and the optimization method once again suggested that the highest levels of  $p$  and  $pfr$  be used. According to Table 10, the optimization method proposed two sets of process parameters based on the experimental campaign centered on solution 1, which has the highest  $P_{st}$ . These differ only in terms of the used  $v$ , indicating that in this parameter range,  $v$  has no effect on deposition performance, but only the shape and dimensions of the clad. To assess this, both proposed  $v$  values were tested on thick walls. Anyway, as previously discussed and as shown in .

Table 11, the lowest level of  $v$  was proposed for the solution with the highest  $E_{st}$ .

The thick wall depositions with the three optimized process conditions outperform the corresponding single-track depositions. This is true even for depositions with process parameters derived from Solution 2 of the refinement campaign, even though it indicated an almost unimprovable level of  $E_{tw}$ . In fact, the results obtained with the thick walls are promising, with various process conditions achieving deposition rates of around 1100 g/h with a waste of only about 10% of the delivered powder.

These process parameter sets outperform the deposition rate commonly associated with C-LMD processes. According to the literature, the productivity of the C-LMD process with powder is around 300–500 g/h, and in order to achieve the so-called HDR-LMD, very large laser spots ( $\varnothing > 4$  mm, up to 9 mm) and much higher levels of  $p$  ( $p > 3000$  W, up to 7500 W) are required [10]. In terms of powder catchment efficiency, it is commonly assumed that C-LMD wastes a significant amount of powder. These results show indeed that with a proper optimization of the process, particularly good results can be achieved even with a C-LMD setup. The selection of process parameters that generate clads with  $\alpha < 60^\circ$  proved to be a successful method of preventing lack of fusion porosity between adjacent tracks in fully dense multi-pass multi-layer depositions. As a result, the hypothesis regarding the direct

applicability on thick walls of process conditions optimized on single track was proven to be correct, allowing optimization procedures to be run on single tracks rather than thick walls, with remarkable convenience and reliability.

The correct combination of 3D geometrical parameters, namely the hatch spacing  $hs$  and the Z-step  $Zs$ , proved to be critical for ensuring a successful built while avoiding undergrowth and overgrowth issues. Furthermore, if properly balanced, process performance is not hampered. This observation suggests that by adjusting  $hs$  and  $Zs$ , the thick wall width and height can be tuned without sacrificing deposition rate. It should be noted, however, that the process windows for the 3D geometrical parameters are quite narrow, making this an aspect that should be carefully addressed during the optimization procedure. Finally, it was shown that  $v$  had no effect on process performance, at least in the tested range. This was also noticed during the initial optimization step on single tracks. This discovery, if confirmed for a wider range of process conditions, is valuable because it allows for clad shape manipulation without altering process performance. This proved especially useful in the final stages of the optimization procedure, which aimed to increase the deposition rate even further. Indeed, as previously stated, the tested process conditions are close to the limit of the evaluated range, implying that, if possible, pushing the process parameters beyond these limits may improve process performance. In any case, for the chosen setup,  $p$  was already close to the maximum allowable level of 2000 W. As a result, it was only set to its maximum for the following steps. Although increasing  $p$  further would have been possible, the intensity of the laser on the working plane may be too high if the laser spot is not also enlarged, which may impair deposition stability. This issue was not addressed in this work.

Another recurring observation made in this work is that both the productivity  $P$  and the powder catchment efficiency  $E$  are generally higher in thick walls with respect to the correspondent single track. In simpler terms:  $P_{tw} > P_{st}$  and  $E_{tw} > E_{st}$  when using the same process parameter sets. This phenomenon has been noted in earlier investigations as well. One plausible explanation is that during deposition of multi-track layers, the powder stream is partially reflected by the presence of the previously deposited solid track, and it is more likely to feed the molten pool. Conversely, when depositing a single track, the powder stream encounters no lateral barriers that would prevent particles from escaping the deposition zone [38, 39, 56]. Additionally, another explanation arises from the continuous deposition of subsequent tracks, resulting in the accumulation of heat within the underlying material. This rise in temperature fosters the growth of the molten pool, as it necessitates less energy to reach the melting point of the supplied material [32, 52, 56]. This effect is similar to applying preheating to the substrate.

In terms of the knowledge gained from the single tracks deposited for the initial optimization campaign, increasing

$pfr$  should increase  $P_{st}$ , but it should also increase  $\alpha$ . It was also demonstrated that too much steepness is causing the formation of inter-run lack of fusion porosity between adjacent clads, which should be avoided. Simply increasing the  $pfr$  resulted in  $P_{tw}$  of about 1600 g/h and  $E_{tw}$  of about 76%. The material, however, was not completely dense. The role of  $v$  in this optimization campaign was vital, as its adjustment solved the porosity problem with only a minor reduction in process performance. The final accepted process condition for IN718, which produced structures free of pores, was 1500 g/h deposition rate  $P_{tw}$  and 70% powder catchment efficiency  $E_{tw}$  (i.e., only 30% of delivered powder is wasted).

The results obtained throughout this work highlight the fact that the C-LMD process with powder arguably has a huge potential that can still be exploited by setting up a proper optimization strategy.

## 6 Conclusions

This paper concludes a two-part work on the analysis and optimization of the process performance (i.e., the productivity and the powder catchment efficiency) of C-LMD with powder of IN718. In Part I, a wide experimental campaign was conducted on single tracks and established the fundamental effects of the process parameters which govern the productivity and efficiency of the process. The knowledge acquired in Part I is refined and applied in Part II on further experimentations on both single tracks and thick walls.

- The sets of parameters obtained with the optimization procedure run on single tracks proved to be effective in the deposition of multi-pass multi-layer thick walls, on which only the hatch spacing and the Z-step should be tuned to avoid process drifts. In this way, fully dense thick walls were deposited with productivity of about 1100 g/h and powder catchment efficiency of 90%.
- Using the knowledge gained about the process behavior in response to process parameters, it was possible to achieve the deposition of fully dense thick-walled specimens at around 1500 g/h and 70% productivity and efficiency, respectively. By raising both the powder feed rate and the scan speed, the desired result was reached.
- The role of scan speed was critical for this optimization procedure because it only affects the shape and size of the clad and not the process performance. It was successfully employed to regulate the lack of fusion holes induced by an increase in powder feed rate without impacting the achieved deposition rate or efficiency.

The achieved performance is significantly higher than what is commonly known about the process. The results also show that the C-LMD process still has potential for

improvement by finely tuning and optimizing the process parameters, making it more appealing for depositing large components with good performance and high quality of the deposited material. With such results, the industrialization of the C-LMD process is more likely to occur in various fields such as aerospace or oil and gas, for which large one-of-the-kind components made by high-end materials are required.

The approach employed in this study is entirely experimental, relying on statistical process optimization techniques and the utilization of basic analytical formulas to define efficiency and productivity. Nevertheless, the achieved results and the extensive range of experimented parameters establish a robust foundation for further optimization endeavors and for more comprehensive quality investigations through numerical models of the LMD process. Other future developments of this study could include the adaptation of the approach to other materials that are more difficult to print than IN718. Finally, the proposed approach for the optimization could be applied on other directed energy deposition technologies, including HDR-LMD with larger laser spots and/or higher laser power, as well as wire-based processes.

**Abbreviations** 3D: Three-dimensional; AM: Additive manufacturing; ANOVA: Analysis of variance; C-LMD: Conventional laser metal deposition; CNC: Computer numerical control;  $E$ , [%]: Powder catchment efficiency; EHLA: Extreme high speed laser application;  $E_{st}$ , [%]: Single track powder catchment efficiency;  $E_{tw}$ , [%]: Thick wall powder catchment efficiency;  $h$ , [mm]: Single track height;  $H$ , [mm]: Thick wall height; HDR-LMD: High deposition rate laser metal deposition;  $hs$ , [mm]: Hatch spacing; IN718: Inconel 718;  $l$ , [mm]: Length of acquired portion of single track;  $L$ , [mm]: Length of the thick wall; LC: Laser cladding; LMD: Laser metal deposition; LPBF: Laser powder bed fusion;  $N_{il}$ , [-]: Number of oblique infill lines;  $N_{la}$ , [-]: Number of layers;  $P$ , [g/h]: Productivity/deposition rate;  $p$ , [W]: Laser power;  $pfr$ , [g/h]: Powder feed rate;  $P_{st}$ , [g/h]: Single track productivity/deposition rate;  $P_{tw}$ , [g/h]: Thick wall productivity/deposition rate;  $sod$ , [mm]: Standoff distance;  $t$ , [s]: Deposition time;  $t_{tw}$ , [s]: Thick wall deposition time;  $v$ , [mm/min]: Scan speed;  $V$ , [mm<sup>3</sup>]: Deposited volume;  $V_{st}$ , [mm<sup>3</sup>]: Single track volume;  $V_{tw}$ , [mm<sup>3</sup>]: Thick wall volume;  $w$ , [mm]: Single track width;  $W$ , [mm]: Thick wall width;  $Z_s$ , [mm]: Z-step;  $\alpha$ , [deg]: Single track contact angle;  $\rho$ , [g/cm<sup>3</sup>]: Material density

**Supplementary Information** The online version contains supplementary material available at <https://doi.org/10.1007/s00170-023-12197-0>.

**Acknowledgements** Nuovo Pignone Tecnologie S.R.L. (Baker Hughes) is acknowledged for granting the industrial PhD scholarship which made this research possible, as well as their extensive knowledge and support.

**Author contribution** Simone Maffia: conceptualization, methodology, validation, investigation, visualization, formal analysis, software, writing—original draft, writing—review & editing. Federico Chiappini: conceptualization, methodology, validation, investigation. Gianluca Maggiani: supervision. Valentina Furlan: methodology. Massimo Guerini: supervision, funding acquisition, resources. Barbara Previtali: methodology, investigation, writing—review & editing, supervision, funding acquisition, resources.

**Funding** Open access funding provided by Politecnico di Milano within the CRUI-CARE Agreement.

## Declarations

**Conflict of interest** The authors declare no competing interests.

**Open Access** This article is licensed under a Creative Commons Attribution 4.0 International License, which permits use, sharing, adaptation, distribution and reproduction in any medium or format, as long as you give appropriate credit to the original author(s) and the source, provide a link to the Creative Commons licence, and indicate if changes were made. The images or other third party material in this article are included in the article's Creative Commons licence, unless indicated otherwise in a credit line to the material. If material is not included in the article's Creative Commons licence and your intended use is not permitted by statutory regulation or exceeds the permitted use, you will need to obtain permission directly from the copyright holder. To view a copy of this licence, visit <http://creativecommons.org/licenses/by/4.0/>.

## References

- Blakey-Milner B, Gradl P, Snedden G, Brooks M, Pitot J, Lopez E, Leary M, Berto F, Du Plessis A (2021) Metal additive manufacturing in aerospace: a review. *Mater Des* 209:110008. <https://doi.org/10.1016/j.matdes.2021.110008>
- Jinoop A, Paul C, Bindra K (2019) Laser-assisted directed energy deposition of nickel super alloys: a review. *Proc Inst Mech Eng, Part L: J Mater: Des Appl* 233:2376–2400. <https://doi.org/10.1177/1464420719852658>
- Tarancón A, Esposito V, Torrell M, Vece MD, Son JS, Norby P, Barg S, Grant PS, Vogelpoth A, Linnenbrink S, Brucki M, Schopphoven T, Gasser A, Persembe E, Koufou D, Kuhn S, Ameloot R, Hou X, Engelbrecht K, Bahl CRH, Pryds N, Wang J, Tsouris C, Miramontes E, Love L, Lai C, Sun X, Kærn MR, Criscuolo G, Pedersen DB (2022) roadmap on 3D printing for energy. *J Phys Energy* 4:011501. <https://doi.org/10.1088/2515-7655/ac483d>
- Taddese G, Durieux S, Duc E (2020) Sustainability performance indicators for additive manufacturing: a literature review based on product life cycle studies. *Int J Adv Manuf Technol* 107:3109–3134. <https://doi.org/10.1007/s00170-020-05249-2>
- Gradl P, Tinker DC, Park A, Mireles OR, Garcia M, Wilkerson R, McKinney C (2022) Robust metal additive manufacturing process selection and development for aerospace components. *J Mater Eng Perform*. <https://doi.org/10.1007/s11665-022-06850-0>
- Zhang Y, Wu L, Guo X, Kane S, Deng Y, Jung Y-G, Lee J-H, Zhang J (2018) Additive manufacturing of metallic materials: a review. *J Mater Eng Perform* 27:1–13. <https://doi.org/10.1007/s11665-017-2747-y>
- Armstrong M, Mehrabi H, Naveed N (2022) An overview of modern metal additive manufacturing technology. *J Manuf Process* 84:1001–1029. <https://doi.org/10.1016/j.jmapro.2022.10.060>
- Motas JG, Gorji NE, Nedelcu D, Brabazon D, Quadri F, SEM XPS (2021) DSC and nanoindentation characterization of silver nanoparticle-coated biopolymer pellets. *Appl Sci* 11:7706. <https://doi.org/10.3390/app11167706>
- Li Z, Ma X, Zhong C, Sui S, Gasser A, Chen J (2022) Microstructure homogeneity and mechanical property improvement of Inconel 718 alloy fabricated by high-deposition-rate laser directed energy deposition. *Mater Sci Eng* 832:142430. <https://doi.org/10.1016/j.msea.2021.142430>
- Li Z, Sui S, Ma X, Tan H, Zhong C, Bi G, Clare AT, Gasser A, Chen J (2022) High deposition rate powder- and wire-based laser directed energy deposition of metallic materials: a review. *Int J Mach Tools Manuf* 181:103942. <https://doi.org/10.1016/j.ijmactools.2022.103942>
- Li Z, Chen J, Sui S, Zhong C, Lu X, Lin X (2020) The microstructure evolution and tensile properties of Inconel 718 fabricated by high-deposition-rate laser directed energy deposition. *Additive Manufacturing*. 31:100941
- Zhong C, Gasser A, Backes G, Fu J, Schleifenbaum JH (2022) Laser additive manufacturing of Inconel 718 at increased deposition rates. *Mater Sci Eng* 844:143196. <https://doi.org/10.1016/j.msea.2022.143196>
- Sui S, Li Z, Zhong C, Zhang Q, Gasser A, Chen J, Chew Y, Bi G (2021) Laves phase tuning for enhancing high temperature mechanical property improvement in laser directed energy deposited Inconel 718. *Compos Part B: Eng* 215:108819. <https://doi.org/10.1016/j.compositesb.2021.108819>
- Kittel J, Gasser A, Wissenbach K, Zhong C, Schleifenbaum JH, Palm F (2020) Case study on AM of an IN718 aircraft component using the LMD process. *Procedia CIRP* 94:324–329. <https://doi.org/10.1016/j.procir.2020.09.061>
- Selcuk C (2011) Laser metal deposition for powder metallurgy parts. *Powder Metall* 54:94–99. <https://doi.org/10.1179/174329011X12977874589924>
- Ma M, Wang Z, Zeng X (2015) Effect of energy input on microstructural evolution of direct laser fabricated IN718 alloy. *Mater Charact* 106:420–427
- Cooke S, Ahmadi K, Willerth S, Herring R (2020) Metal additive manufacturing: technology, metallurgy and modelling. *J Manuf Process* 57:978–1003. <https://doi.org/10.1016/j.jmapro.2020.07.025>
- Yan Z, Liu W, Tang Z, Liu X, Zhang N, Li M, Zhang H (2018) Review on thermal analysis in laser-based additive manufacturing. *Opt Laser Technol* 106:427–441. <https://doi.org/10.1016/j.optlastec.2018.04.034>
- Ngo TD, Kashani A, Imbalzano G, Nguyen KTQ, Hui D (2018) Additive manufacturing (3D printing): a review of materials, methods, applications and challenges. *Compos B Eng* 143:172–196. <https://doi.org/10.1016/j.compositesb.2018.02.012>
- Li T, Zhang L, Bultel GGP, Schopphoven T, Gasser A, Schleifenbaum JH, Poprawe R (2019) Extreme high-speed laser material deposition (EHLA) of AISI 4340 steel. *Coatings* 9:778. <https://doi.org/10.3390/coatings9120778>
- Liang Y, Liao ZY, Zhang LL, Cai MW, Wei XS, Shen J (2023) A review on coatings deposited by extreme high-speed laser cladding: processes, materials, and properties. *Opt Laser Technol* 164:109472. <https://doi.org/10.1016/j.optlastec.2023.109472>
- Schaible J, Hausch D, Schopphoven T, Häfner C (2022) Deposition strategies for generating cuboid volumes using extreme high-speed directed energy deposition. *J Laser Appl* 34:042034. <https://doi.org/10.2351/7.0000770>
- Shamsaei N, Yadollahi A, Bian L, Thompson SM (2015) An overview of Direct Laser Deposition for additive manufacturing. Part II: Mech Behav, Process Parameter Optim Control, *Addit Manuf* 8:12–35. <https://doi.org/10.1016/j.addma.2015.07.002>
- Masaylo D, Igoshin S, Popovich A, Popovich V (2020) Effect of process parameters on defects in large scale components manufactured by direct laser deposition. *Mater Today: Proc* 30:665–671. <https://doi.org/10.1016/j.matpr.2020.01.519>
- Sreekanth S, Ghassemali E, Hurtig K, Joshi S, Andersson J (2020) Effect of direct energy deposition process parameters on single-track deposits of alloy 718. *Metals* 10:96
- Zhong C, Chen J, Gasser A, Sui S, Schleifenbaum JH (2018) Microstructures, tensile properties, and fracture mechanisms of Inconel 718 formed by HDR-LMD with PREP and GA powders.

- Int J Adv Manuf Technol 96:2031–2041. <https://doi.org/10.1007/s00170-018-1662-1>
27. Mazzucato F, Aversa A, Doglione R, Biamino S, Valente A, Lombardi M (2019) Influence of process parameters and deposition strategy on laser metal deposition of 316L powder. *Metals* 9:1160. <https://doi.org/10.3390/met9111160>
  28. Mvolo E, Sabourin L, Boisselier D (2023) An investigation of key parameters in metal additive manufacturing for robotic paths planning of large parts, *Weld. World* 67:873–883. <https://doi.org/10.1007/s40194-023-01487-6>
  29. Chang Y-Y, Qiu J-R, Hwang S-J (2022) Multi-objective optimization of directed energy deposition process by using Taguchi-Grey relational analysis. *Int J Adv Manuf Technol* 120:7547–7563. <https://doi.org/10.1007/s00170-022-09210-3>
  30. Liang Y-J, Li J, Li A, Cheng X, Wang S, Wang H-M (2017) Experimental optimization of laser additive manufacturing process of single-crystal nickel-base superalloys by a statistical experiment design method. *J Alloys Compd* 697:174–181
  31. Jardon Z, Ertveldt J, Hinderdael M, Guillaume P (2021) Process parameter study for enhancement of directed energy deposition powder efficiency based on single-track geometry evaluation. *J Laser Appl* 33:042023. <https://doi.org/10.2351/7.0000516>
  32. Pellizzari M, Zhao Z, Bosetti P, Perini M (2022) Optimizing direct laser metal deposition of H13 cladding on CuBe alloy substrate. *Surf Coatings Technol* 432:128084. <https://doi.org/10.1016/j.surfcoat.2022.128084>
  33. Lin P-Y, Shen F-C, Wu K-T, Hwang S-J, Lee H-H (2020) Process optimization for directed energy deposition of SS316L components. *Int J Adv Manuf Technol* 111:1387–1400. <https://doi.org/10.1007/s00170-020-06113-z>
  34. Carrozza A, Mazzucato F, Aversa A, Lombardi M, Bondioli F, Biamino S, Valente A, Fino P (2021) Single scans of Ti-6Al-4V by directed energy deposition: a cost and time effective methodology to assess the proper process window. *Met Mater Int* 27:3590–3602. <https://doi.org/10.1007/s12540-020-00930-3>
  35. Bax B, Rajput R, Kellet R, Reisacher M (2018) Systematic evaluation of process parameter maps for laser cladding and directed energy deposition. *Addit Manuf* 21:487–494
  36. Odum K, Leung L, Soshi M, Yamazaki K (2022) Improvement of directed energy deposition (DED) material addition rate via fluence-based parameter scaling method. *Prog Addit Manuf* 7:127–137. <https://doi.org/10.1007/s40964-021-00220-3>
  37. Dalae M, Cerrutti E, Dey I, Leinenbach C, Wegener K (2022) Parameters development for optimum deposition rate in laser DMD of stainless steel EN X3CrNiMo13-4. *Lasers Manuf Mater Process* 9:1–17. <https://doi.org/10.1007/s40516-021-00161-3>
  38. Koti D, Powell J, Voisey KT (2022) Improving laser cladding productivity with 'ABA' cladding. *Procedia CIRP* 111:205–209. <https://doi.org/10.1016/j.procir.2022.08.048>
  39. Koti D, Powell J, Naestroem H, Voisey KT (2023) Powder catchment efficiency in laser cladding (directed energy deposition). An investigation into standard laser cladding and the ABA cladding technique. *J Laser Appl* 35:012025. <https://doi.org/10.2351/7.0000904>
  40. Peng T, Kellens K, Tang R, Chen C, Chen G (2018) Sustainability of additive manufacturing: an overview on its energy demand and environmental impact. *Addit Manuf* 21:694–704. <https://doi.org/10.1016/j.addma.2018.04.022>
  41. Powell J, Koti D, Garmendia X, Voisey KT (2023) Assessing the quality and productivity of laser cladding and direct energy deposition: guidelines for researchers. *J Laser Appl* 35:012024. <https://doi.org/10.2351/7.0000897>
  42. Wang HP, Zheng CH, Zou PF, Yang SJ, Hu L, Wei B (2018) Density determination and simulation of Inconel 718 alloy at normal and metastable liquid states. *J Mater Sci Technol* 34:436–439. <https://doi.org/10.1016/j.jmst.2017.10.014>
  43. Donadello S, Furlan V, Demir AG, Previtali B (2022) Interplay between powder catchment efficiency and layer height in self-stabilized laser metal deposition. *Opt Lasers iEng* 149:106817. <https://doi.org/10.1016/j.optlaseng.2021.106817>
  44. Lin J (2000) Laser attenuation of the focused powder streams in coaxial laser cladding. *J Laser Appl* 12:28–33. <https://doi.org/10.2351/1.521910>
  45. de Oliveira U, Ocelík V, De Hosson JThM (2005) Analysis of coaxial laser cladding processing conditions. *Surf Coat Technol* 197:127–136. <https://doi.org/10.1016/j.surfcoat.2004.06.029>
  46. Gharbi M, Peyre P, Gorny C, Carin M, Morville S, Le Masson P, Carron D, Fabbro R (2013) Influence of various process conditions on surface finishes induced by the direct metal deposition laser technique on a Ti-6Al-4V alloy. *J Mater Proc Technol* 213:791–800
  47. Liu S, Kovacevic R (2014) Statistical analysis and optimization of processing parameters in high-power direct diode laser cladding. *Int J Adv Manuf Technol* 74:867–878. <https://doi.org/10.1007/s00170-014-6041-y>
  48. Marzban J, Ghaseminejad P, Ahmadzadeh MH, Teimouri R (2015) Experimental investigation and statistical optimization of laser surface cladding parameters. *Int J Adv Manuf Technol* 76:1163–1172. <https://doi.org/10.1007/s00170-014-6338-x>
  49. Maffia S, Chiappini F, Maggiani G, Furlan V, Guerrini M, Previtali B (2023) Comparison between eight-axis articulated robot and five-axis CNC gantry laser metal deposition machines for fabricating large components. *Appl Sci* 13:5259. <https://doi.org/10.3390/app13095259>
  50. Schneider CA, Rasband WS, Eliceiri KW (2012) NIH Image to ImageJ: 25 years of image analysis. *Nat Methods* 9:671–675. <https://doi.org/10.1038/nmeth.2089>
  51. Maffia S, Finazzi V, Berti F, Migliavacca F, Petrini L, Previtali B, Demir AG (2021) Selective laser melting of NiTi stents with open-cell and variable diameter. *Smart Mater Struct* 30:105010. <https://doi.org/10.1088/1361-665X/ac1908>
  52. Ocelík V, Nenadl O, Palavra A, De Hosson JThM (2014) On the geometry of coating layers formed by overlap. *Surf Coat Technol* 242:54–61
  53. Zhang H, Zhu L, Xue P (2020) Laser direct metal deposition of variable width thin-walled structures in Inconel 718 alloy by coaxial powder feeding. *Int J Adv Manuf Technol* 108:821–840
  54. Ilanlou M, Razavi RS, Haghghat S, Nourollahi A (2023) Multi-track laser metal deposition of Stellite6 on martensitic stainless steel: geometry optimization and defects suppression. *J Manuf Proc* 86:177–186. <https://doi.org/10.1016/j.jmapro.2022.12.036>
  55. Nenadl O, Ocelík V, Palavra A, Hosson JThMD (2014) The prediction of coating geometry from main processing parameters in laser cladding. *Phys Procedia* 56:220–227
  56. dos Santos Paes LE, Ferreira HS, Pereira M, Xavier FA, Weingaertner WL, Vilarinho LO (2021) Modeling layer geometry in directed energy deposition with laser for additive manufacturing. *Surf Coat Technol* 409:126897. <https://doi.org/10.1016/j.surfcoat.2021.126897>
  57. Caiazza F (2018) Laser-aided directed metal deposition of Ni-based superalloy powder. *Opt Laser Technol* 103:193–198. <https://doi.org/10.1016/j.optlastec.2018.01.042>
  58. Mazzarisi M, Errico V, Angelastro A, Campanelli SL (2022) Influence of standoff distance and laser defocusing distance on direct laser metal deposition of a nickel-based superalloy. *Int J Adv Manuf Technol*. <https://doi.org/10.1007/s00170-022-08945-3>

**Publisher's Note** Springer Nature remains neutral with regard to jurisdictional claims in published maps and institutional affiliations.